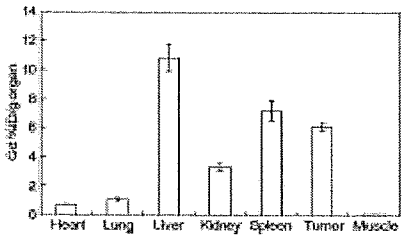

Fig. 5. Biodistribution of PEG-P(Lys-DOTA-Gd) micelle 24 h after injection at a dose of 0.03 mmol Gd/kg.

observations. The blood concentrations of the polymeric micelles were measured by means of ICP. Fig. 4 shows the blood concentration-time course of the polymeric micelles until 48 h after the injection. A low-molecular-weight gadolinium ion complex, such as Gd–DTPA, was immediately excreted 1 h after injection (only 1.4 ± 0.8% was found in blood). On the other hand, the polymeric micelle remained 22.5 ± 2.9% and 10.2 ± 1.4% (mean ± SD) in blood at 24 h and 48 h after the injection, respectively. These high blood concentrations exhibit significantly stable circulation of the polymeric micelle in blood. This polymeric micelle underwent an approximately 10-fold dilution relative to the injection in blood; however, stable formation of the polymeric micelle at such diluted conditions was confirmed in this in vivo experiment. This stable blood-circulation time-course was similar to the system of anti-cancer drug-incorporating polymeric micelle, a doxorubicin-incorporating poly(ethylene glycol)-b-poly (aspartic acid) system [1]. According to reports, the doxorubicin-incorporating polymeric micelle system provides a drug concentration of 24.6% of the injected dose (ID) after 24 h in the blood. Such a long circulating property of the doxorubicin-incorporating polymeric micelle successfully led to highly selective tumor accumulation. Owing to this similar pharmacokinetic behavior, this MRI contrast agent can be a strong tool for estimation of the pharmacokinetic behavior of "anti-cancer drug"-incorporating polymeric micelles.

3.3. *Biodistribution and excretion of the polymeric micelle MRI contrast agent*

Selective and high accumulation of drug carriers at solid tumors is essential for an improvement of anticancer drug efficacy. As well as the drug-targeting systems, selective and high accumulation is desired for diagnostic agents.

In recent decades, polymeric micelles have constituted one of the best drug-carriers to have achieved selective accumulation of an anti-cancer drug, through the EPR effect, at solid tumor tissues [1]. Biodistribution of the polymeric micelle contrast agents was evaluated in CDF_1 female mice bearing the colon 26 tumor. Fig. 5 shows the percentage of the injected dose of the polymeric micelle 24 h after the injection in the normal organs as well as in tumor tissues. The study showed that the accumulation of the polymeric micelle contrast agent in tumor tissues reached 6.1 ± 0.3% ID (injected dose)/g of tumor. This accumulation amount was considerably high. Furthermore, highly selective delivery was present with low accumulation amounts in heart, kidney, and muscle tissue. For the mononuclear phagocyte system (MPS), this contrast agent was found to be accumulated in 10.8 ± 0.9 and 7.2 ± 0.7% ID/g of liver and spleen, respectively. These accumulation ratios were similar to those in case of doxorubicin-incorporated polymeric micelle, but better tumor/muscle ratios were obtained in this MRI contrast agent [1]. This difference may rest on a difference in micelle size as well as in detection species; there is a physically entrapped drug for the drug-carrying micelles and there are chelated gadolinium ions for the MRI contrast agent. The gadolinium-binding macromolecular

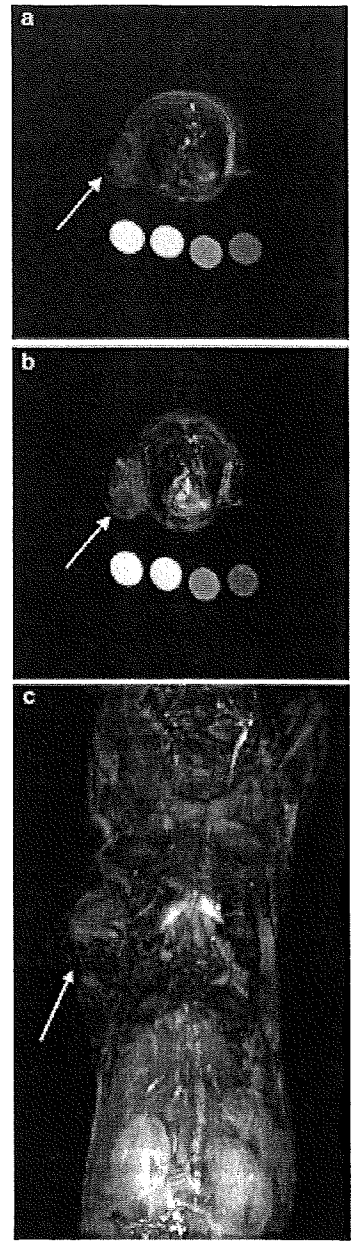

Fig. 6. Axial slices of MR images (a) before and (b) 24 h after the injection at a dose of 0.03 mmol Gd/kg. Tumor areas are on the left side in the axial slices. The circles indicate the stock solutions of (left to right) 1.0 mM, 0.5 mM, 0.1 mM gadolinium ion in agarose gel and blank in agarose gel. T_1-weighted gradient echo protocol was used. Parameters of the T_1-weighted images were TR/TE = 80/4.6, flip angle = 30°, field of view of 45 × 45 mm, a matrix size of 192 × 192, and 2 mm of axial slice thickness. Arrows indicate tumor tissue. (c) MIP images of coronal slices 24 h after injection. Arrow indicates tumor. Parameters of the T_1-weighted images were TR/TE = 80/4.2, flip angle = 30°, field of view of 50 × 30 mm, a matrix size of 192 × 192. MIP images were obtained by 2 mm thickness × 4 slices.

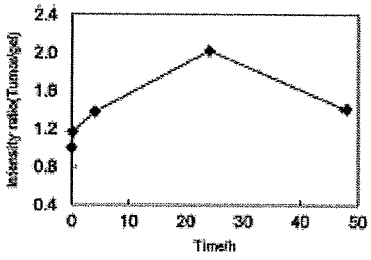

Fig. 7. Relative signal intensities of tumor area at defined time (0 h, 4 h, 24 h, 48 h) after the injection of the polymeric micelle MRI contrast agent.

carrier may not penetrate into muscle as do low-"molecular weight" drugs that are released from the carrier.

Wang Y et al. reported that poly[N-(2-hydroxypropyl)methacrylamide] (PHPMA) [14] gadolinium-conjugates exhibited size-dependent tumor accumulation. They stated that a large molecular weight of PHPMA (121 kDa) gadolinium conjugate exhibited the best tumor accumulation at 7 days after injection. Although, Bogdanov A et al. reported another example of successful passive targeting to solid tumors with a graft copolymer of poly(ethylene glycol) featuring poly(L-lysine) [9]. This contrast agent exhibited tumor targeting with a long blood-circulation time ($t_{1/2}$= 36 h); however, this long-circulation property in blood indicates that the contrast agent cannot excrete smoothly from the body owing to the polymer's very large molecular weight (690 kDa). The researchers synthesized different molecular weights of similar polymers to compare the polymers' biodistribution [10] and found that the polymers accumulated at solid tumors in a "molecular-weight"-dependent manner. This molecular-weight dependency indicated that smaller molecular weights of polymers can be excreted through the kidneys.

These above-mentioned polymers exhibited better tumor accumulation, corresponded to larger molecular weights of the polymers. However, the excretion of the contrast agent, especially in the case of the macromolecular contrast agent, is a serious matter for the development of diagnostic agents.

Therefore, we checked the kidneys' excretion of our polymeric micelle contrast agent. In urine, 20.8 ± 7.6% of the polymeric micelle was found 48 h after the injection. This result indicates that the polymeric micelle was excreted through the kidney filtration. Since the size of the polymeric micelle contrast agent was 50–250 nm as shown in Fig. 3(a), the polymeric micelles cannot pass through the kidney filtration. Therefore, these polymers that formed in urine appears to have passed through the kidney filtration in a dissociated polymer form, since the average molecular weight of this block copolymer is only 15,000. This is an excellent property of the polymeric micelle MRI contrast agent; namely, this agent exhibits long circulation in blood in a micelle form, while this agent can be excreted through the kidneys in a dissociated polymer form.

Furthermore, the obtained polymeric micelle MRI contrast agent delivered a larger amount to solid tumors than did previously reported macromolecular MRI contrast agents that can be also excreted from the kidneys (agents such as PHPMA gadolinium-conjugate [14] and graft copolymer of poly(ethylene glycol) with poly (L-lysine) [10]).

In order to estimate possible acute toxicity, we injected the 4-fold of the volume of the contrast agent into the mouse tail vein, and observed the body weight change over the course of 16 days. There was no significant difference in comparison to the control (less than ± 10%). Although we have to conduct further experiments to obtain toxicity-related information of greater exactness, these preliminary results indicate that this polymeric micelle can dissociate and be excreted from the kidneys, and that this tumor targeting results a passive targeting mechanism (the EPR effect). In a future study, we would like to optimize the pharmacokinetics and the dissociation behavior of the polymeric micelles by controlling the composition of the block copolymers.

3.4. MR imaging at tumor tissue

We took an MR image of the tumor-bearing mouse after the injection of the polymeric micelle contrast agent. Fig. 6 shows T_1-weighted MR images of tumor tissues before and after 24 h at an injection dose of 0.05 mmol Gd/kg. After the injection of the polymeric micelle, MR images exhibited a significant signal enhancement at the kidneys. This signal enhancement at the kidneys indicates that kidneys excreted the contrast agent, as shown in Fig. 6(c). However, even 24 h after the injection, an intense signal was observed in the heart and aorta areas. This indicates that a considerable amount of the contrast agent was circulating in the bloodstream, as described in pharmacokinetic results. The relative signal intensity at axial slices of the tumor tissues underwent a 2.0-fold increase after 24 h, as compared with the signal before the injection. The signal intensity of the tumor area had gradually increased by 24 h and had slightly decreased by 48 h, as shown in Fig. 7. This behavior of the signal intensities is similar to the doxorubicin concentration delivered by the polymeric micelle carrier system. All these results indicate that the enhancement of MR signals in the tumor area rested on the successful passive accumulation of the MRI contrast agent at solid tumors.

4. Conclusion

We prepared polymeric micelle MRI contrast agents using poly (ethylene glycol)-*b*-poly(L-lysine) block copolymers. A reaction of poly(ethylene glycol)-*b*-poly(L-lysine) with a DOTA derivative resulted in a quantitative DOTA conjugation regarding the lysine residues of the block copolymer, and the obtained block copolymer formed a polymeric micelle. This micellar structure was maintained after a partial chelation of the DOTA moiety with gadolinium ions. The biodistribution and the excretion of the polymeric micelle was evaluated in colon 26-bearing CDF_1 female mice. Selective accumulation of the polymeric micelle at the tumor tissues was observed 24 h after the injection. The contrast agent's accumulation substantially enhanced the signal intensity of the MR images at the tumor. This polymeric micelle MRI contrast agent will be a useful diagnostic tool, particularly in combination with a polymeric micelle-based drug-targeting system.

Acknowledgement

This work was supported by the Ministry of Health, Labour, and Welfare of Japan. K. Shiraishi and M. Yokoyama acknowledge the support from the Program for Promoting the Establishment of Strategic Research Centers, Special Coordination Funds for Promoting Science and Technology, the Ministry of Education, Culture, Sports, Science and Technology of Japan, and Tokyo Ohka Foundation for the Promotion of Science and Technology.

Appendix A. Supplementary data

Supplementary data associated with this article can be found, in the online version, at doi:10.1016/j.jconrel.2009.01.010.

References

[1] M. Yokoyama, T. Okano, Y. Sakurai, S. Fukushima, K. Okamoto, K. Kataoka, Selective delivery of adriamycin to a solid tumor using a polymeric micelle carrier system, J. Drug Target. 7 (3) (1999) 171–186.

[2] Y. Matsumura, H. Maeda, A new concept for macromolecular therapeutics in cancer chemotherapy: mechanism of tumoritropic accumulation of proteins and the antitumor agent Smancs, Cancer Res. 46 (1986) 6387–6392.
[3] H.M. Allahdadi, A. Lavasanifar, Polymeric micelles for drug delivery, Expert Opin. Drug Deliv. 3 (1) (2006) 130–162.
[4] N. Nishiyama, S. Okazaki, H. Cabral, M. Miyamoto, Y. Kato, Y. Sugiyama, K. Nishio, Y. Matsumura, K. Kataoka, Novel cisplatin-incorporated polymeric micelles can eradicate solid tumors in mice, Cancer Res. 63 (2003) 8977–8983.
[5] N. Nishiyama, M. Yokoyama, T. Aoyagi, T. Okano, Y. Sakurai, K. Kataoka, Preparation and characterization of self-assembled polymer–metal complex micelle from cis-dichlorodiammineplatinum(II) and poly(ethylene glycol)-poly(α,β-aspartic acid) block copolymer in an aqueous medium, Langmuir 15 (1999) 377–383.
[6] A. Bogdanov Jr, C. Martin, A.V. Bogdanova, T.J. Brady, R. Weissleder, An adduct of cis-diamminedichloroplatinum (II) and poly(ethylene glycol)/poly(L-lysine)-succinate: synthesis and cytotoxic properties, Bioconjug. Chem. 7 (1) (1996) 144–149.
[7] R. Rebizak, M. Schaefer, E. Dellacherie, Polymeric conjugates of Gd^{3+}-diethylenetriaminepentaacetic acid and dextran. 1. Synthesis, characterization, and paramagnetic properties, Bioconjug. Chem. 8 (4) (1997) 605–610.
[8] M.M. Rieter, A.B. Staubli, K. Kurzedjo, M.H.B. Gray, J. Shih, S.E. Fraser, R.E. Jacobs, T.J. Meade, Fluorescently detectable magnetic resonance imaging agents, Bioconjug. Chem. 9 (2) (1998) 242–249.
[9] A. Bogdanov Jr, S.C. Wright, E.M. Marecos, A.V. Bogdanova, C. Martin, R. Weissleder, A long-circulating co-polymer in "passive targeting" to solid tumors, J. Drug Target. 4 (5) (1997) 321–330.
[10] R. Weissleder, A. Bogdanov Jr, C-H. Tung, H-J. Weinmann, Size optimization of synthetic graft copolymers for in vivo angiogenesis imaging, Bioconjug. Chem. 12 (2) (2001) 213–219.
[11] F. Ye, T. Ke, E-K. Jeong, X. Wang, Y. Sun, M. Johnson, Z-R. Lu, Noninvasive visualization of in vivo drug delivery of poly(L-glutamic acid) using contrast-enhanced MRI, Mol. Pharm. 3 (5) (2006) 507–515.
[12] X. Wen, E.F. Jackson, R.E. Price, E.E. Kim, Q. Wu, S. Wallace, C. Charnsangavej, J.G. Gelovani, C. Li, Synthesis and characterization of poly(L-glutamic acid) gadolinium chelate: a new biodegradable MRI contrast agent, Bioconjug. Chem. 15 (6) (2004) 1408–1415.
[13] Z-R. Lu, X. Wang, D.L. Parker, R.C. Goodrich, H.R. Buswell, Poly(L-glutamic acid) Gd (III)-DOTA conjugate with a degradable spacer for magnetic resonance imaging, Bioconjug. Chem. 14 (4) (2003) 715–719.
[14] Y. Wang, F. Ye, E-K. Jeong, Y. Sun, D.L. Parker, Z-R. Lu, Noninvasive visualization of pharmacokinetics, biodistribution, and tumor targeting of poly[N-(2-hydroxypropyl)methacrylamide] in mice using contrast enhanced MRI, Pharm. Res. 24 (6) (2007) 1208–1216.
[15] H. Kobayashi, M.W. Brechbiel, Dendrimer-based macromolecular MRI contrast agents: characterization and application, Mol. Imag. 2 (1) (2003) 1–10.
[16] H. Kobayashi, S. Kawamoto, S-K. Jo, H.L. Bryant Jr, M.W. Brechbiel, R.A. Star, Macromolecular MRI contrast agents with small dendrimers: pharmacokinetic differences between sizes and cores, Bioconjug. Chem. 14 (2) (2003) 388–394.
[17] H. Kobayashi, N. Sato, S. Kawamoto, T. Saga, A. Hiraga, T.L. Haque, T. Ishimori, J. Konishi, K. Togashi, M.W. Brechbiel, Comparison of the macromolecular MR contrast agents with ethylenediamine-core versus ammonia-core generation-6 polyamidoamine dendrimer, Bioconjug. Chem. 12 (1) (2001) 100–107.
[18] E. Nakamura, K. Makino, T. Okano, T. Yamamoto, M. Yokoyama, Ap dymeric micelle MRI contrast agent with changeable relaxivity, J. Control. Release 114 (2006) 325–333.
[19] V.P. Torchilin, PEG-based micelles as carriers of contrast agents for different imaging modality, Adv. Drug Deliv. Rev. 54 (2002) 235–252.
[20] G. Zhang, R. Zhang, X. Wen, L. Li, C. Li, Micelles based on biodegradable poly(L-glutamic acid)-b-polylactide with paramagnetic Gd ions chelated to the shell layer as a potential nanoscale MRI-visible delivery, Biomacromolecules 9 (1) (2008) 36–42.
[21] R.Y. Lee, H.W. Jee, S.M. Seo, B.K. Kwak, G. Khang, S.H. Cho, Diethylenetriamine-pentaacetic acid–gadolinium (DTPA-Gd)-conjugated polysuccinimide derivatives as magnetic resonance imaging contrast agents, Bioconjug. Chem. 17 (3) (2006) 700–706.
[22] N. Nasongkla, E. Bey, J. Ren, H. Ai, C. Khemtong, J.S. Guthi, S-F. Chin, A.D. Sherry, D.A. Boothman, J. Gao, Multifunctional polymeric micelles as cancer-targeted, MRI-ultrasensitive drug delivery systems, Nano Lett. 6 (11) (2006) 2427–2430.
[23] Z-R. Lu, F. Ye, A. Vaidya, Polymer platforms for drug delivery and biomedical imaging, J. Control. Release 122 (2007) 269–277.
[24] M. Yokoyama, G.S. Kwon, T. Okano, Y. Sakurai, M. Naito, K. Kataoka, Influencing factors on in vitro micelle stability of adriamycin-block copolymer conjugate, J. Control. Release 28 (1994) 59–65.
[25] Y. Takakura, T. Fujita, M. Hashida, H. Sezaki, Disposition character of macromolecules in tumor-bearing mice, Pharm. Res. 7 (4) (1990) 340–346.
[26] A. Harada, K. Kataoka, Formation of polyion complex micelles in an aqueous milieu from a pair of oppositely-charged block copolymers with poly(ethylene glycol) segments, Macromolecules 28 (15) (1995) 5294–5299.

Wide-Ranging Molecular Mobilities of Water in Active Pharmaceutical Ingredient (API) Hydrates as Determined by NMR Relaxation Times

SUMIE YOSHIOKA, YUKIO ASO, TSUTOMU OSAKO, TORU KAWANISHI

National Institute of Health Sciences, 1-18-1 Kamiyoga, Setagaya-ku, Tokyo 158-8501, Japan

Received 10 October 2007; revised 27 November 2007; accepted 28 November 2007

Published online 6 February 2008 in Wiley InterScience (www.interscience.wiley.com). DOI 10.1002/jps.21294

ABSTRACT: In order to examine the possibility of determining the molecular mobility of hydration water in active pharmaceutical ingredient (API) hydrates by NMR relaxation measurement, spin–spin relaxation and spin–lattice relaxation were measured for the 11 API hydrates listed in the Japanese Pharmacopeia using pulsed ^{1}H-NMR. For hydration water that has relatively high mobility and shows Lorentzian decay, molecular mobility as determined by spin–spin relaxation time (T_2) was correlated with ease of evaporation under both nonisothermal and isothermal conditions, as determined by DSC and water vapor sorption isotherm analysis, respectively. Thus, T_2 may be considered a useful parameter which indicates the molecular mobility of hydration water. In contrast, for hydration water that has low mobility and shows Gaussian decay, T_2 was found not to correlate with ease of evaporation under nonisothermal conditions, which suggests that in this case, the molecular mobility of hydration water was too low to be determined by T_2. A wide range of water mobilities was found among API hydrates, from low mobility that could not be evaluated by NMR relaxation time, such as that of the water molecules in pipemidic acid hydrate, to high mobility that could be evaluated by this method, such as that of the water molecules in ceftazidime hydrate.
 J Pharm Sci 97:4258–4268, 2008
Keywords: NMR relaxation time; dynamics; hydrate; DSC; water vapor sorption isotherm

INTRODUCTION

Correlations between chemical stability and molecular mobility have been demonstrated for various amorphous pharmaceuticals in the solid state.[1] Furthermore, the chemical stability of active pharmaceutical ingredient (API) hydrates is suggested to be correlated with the molecular mobility of water of hydration present in the crystalline structure.[2,3]

Water molecules in API hydrates exhibit a variety of physical states,[4,5] suggesting a range of molecular mobilities; water molecules incorporated into rigid crystalline structures may have low molecular mobility, whereas less rigid structures contain water molecules with greater mobility. Hydration water plays an important role in determining the physical characteristics—such as solubility[6] and flowability—of the API hydrate. Therefore, an understanding of the physical properties of hydration water, such as molecular mobility, is critical in the formulation of API hydrates.

The molecular mobility of water in solids may be determined by various methods, such as dielectric relaxation spectroscopy[7] and FT-Raman

Correspondence to: Sumie Yoshioka (Telephone: 81-3-3700-8547; Fax: 81-3-3707-6950; E-mail: yoshioka@nihs.go.jp)
Journal of Pharmaceutical Sciences, Vol. 97, 4258–4268 (2008)

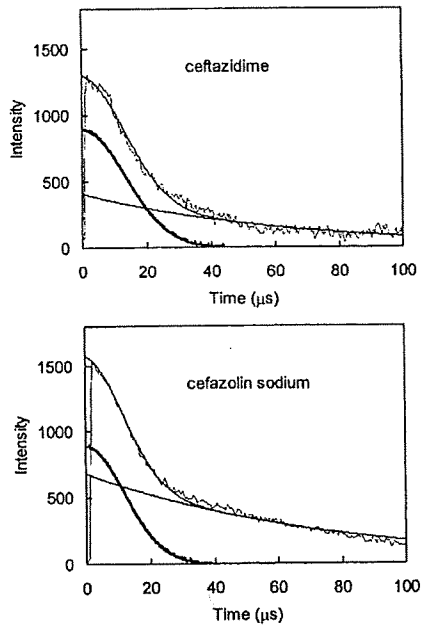

Figure 1. Free induction decay for ceftazidime and cefazolin sodium hydrates.

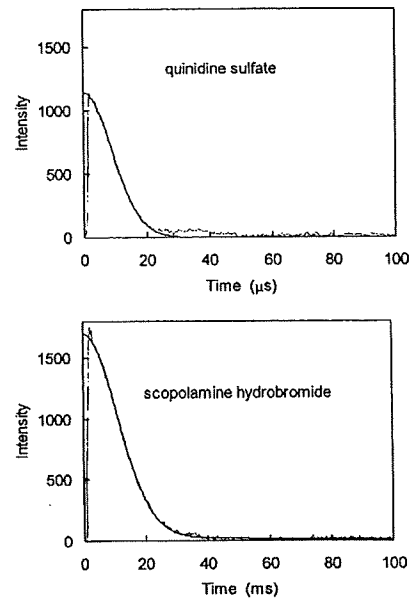

Figure 2. Free induction decay for quinidine sulfate and scopolamine hydrobromide hydrates.

spectroscopy.[8] NMR is also utilized to determine the molecular mobility of water in the solid state,[9] and to examine the various mechanisms by which solids interact with water.[10,11] However, there have been few studies in which the molecular mobility of water in API hydrates was determined using NMR. This may be because ^{1}H-NMR, even high resolution ^{1}H-NMR, cannot separate the peaks of the water protons from those of the protons in other components, which prevents specific determination of water mobility. Although the preparation of API hydrate samples using ^{17}O-labeled water allows to specifically determine the mobility of the water molecules by ^{17}O-NMR, unaffected by the other components, this approach requires high cost and much labor.

Table 1. Water Content of API Hydrates

API Hydrate	Number of H_2O per Molecule Specified in JP	Number of H_2O per Molecule Determined by KF	Spin–Spin Relaxation of H_2O
Cefazolin sodium	5	4.67	Lorentzian
Ceftazidime	5	5.04	Lorentzian
Amoxicillin	3	2.94	Lorentzian
Ampicillin	3	2.96	Lorentzian
Berberine Chloride	Not specified	2.67	Gaussian
Quinine hydrochloride	2	1.31	Gaussian
Scopolamine hydrobromide	3	2.32	Gaussian
Saccharin sodium	2	1.15	Gaussian
Pipemidic acid	3	2.9	Gaussian
Sulpyrine	1	0.98	Gaussian
Quinidine sulfate	2	1.95	Gaussian

DOI 10.1002/jps

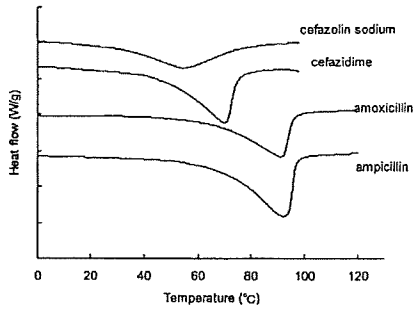

Figure 3. DSC thermograms for four antibiotic hydrates.

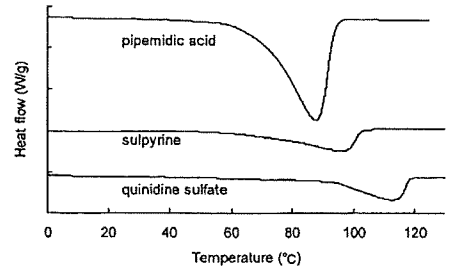

Figure 5. DSC thermograms for API hydrates showing a single endothermic peak.

Thus, determination of the molecular mobility of hydration water in API hydrates using NMR holds some challenges.

However, it is possible to determine the molecular mobility of hydration water in API hydrates by spin–spin relaxation measurement, if the spin–spin relaxation time (T_2) of the water protons is significantly different from that of the API protons. Furthermore, the spin–lattice relaxation time (T_1) of the water protons may be a useful indicator of water mobility, if the ratio of water protons to API protons is sufficiently large, or if the water protons have a correlation time (τ_c) corresponding to the T_1 minimum, such that the T_1 of the water proton is sensitively reflected in the measured T_1 value without being affected by spin diffusion between the water and the API protons. Moreover, even if the ratio of water protons to API protons is not particularly large, and even if water proton does not have a τ_c corresponding to the T_1 minimum, it may be possible to compare the molecular mobility of hydration water in API hydrates based on measured T_1 values, if both of the T_1 of the API proton and the ratio of water protons to API protons are similar for all of the API hydrates compared.

The purpose of this study was to examine the possibility of determining the molecular mobility of hydration water in API hydrates by NMR relaxation measurement. Spin–lattice relaxation, which reflects motions of MHz order, and spin–spin relaxation, which reflects slower motions, were measured for the 11 API hydrates listed in the Japanese Pharmacopeia (JP) using pulsed ^{1}H-NMR, which allows more simplified measurements than high-resolution ^{1}H-NMR. Furthermore, the ease of evaporation of the hydration water was determined under nonisothermal and isothermal conditions using DSC and water vapor sorption isotherm analysis, respectively, and the relationship between the ease of evaporation and the measured values of T_1 and T_2 was examined.

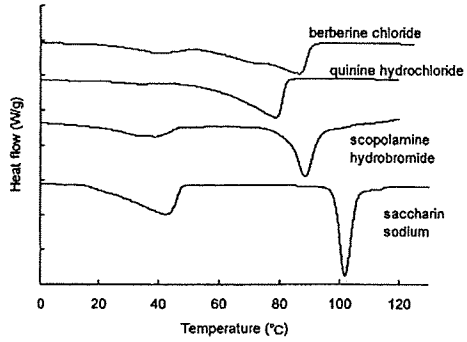

Figure 4. DSC thermograms for API hydrates showing two endothermic peaks.

EXPERIMENTAL

Materials

Cefazolin sodium, ceftazidime, amoxicillin, ampicillin, scopolamine hydrobromide, pipemidic acid, quinidine sulfate hydrates were purchased from Sigma Chemical Co. (St. Louis, MO), and berverine chloride, quinine hydrochloride, saccharin sodium, sulpyrine and di-sodium hydrogen phosphate 12 H_2O were purchased from Wako Pure Chemical Ind. Ltd. (Osaka, Japan), and di-sodium hydrogen phosphate 2 H_2O was from Merck (Darmstadt, Germany).

DOI 10.1002/jps

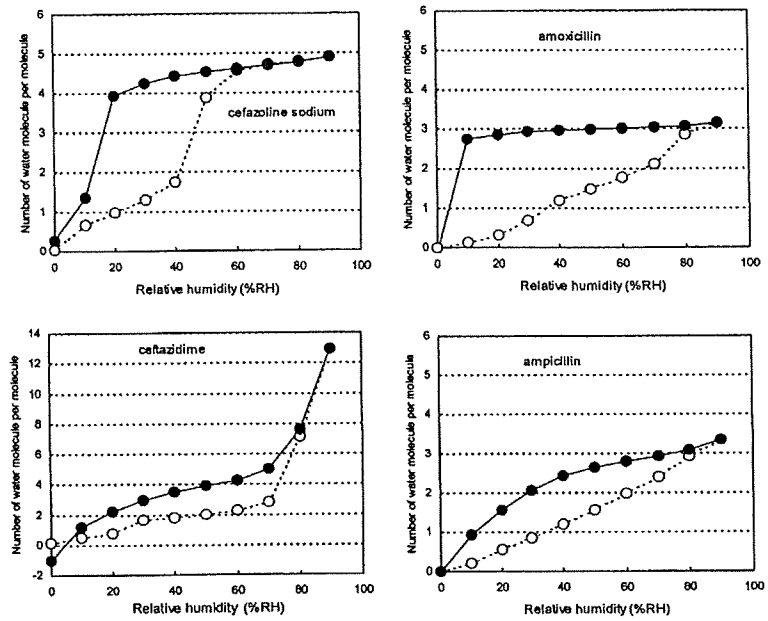

Figure 6. Water sorption isotherms for four antibiotic hydrates.

NMR Relaxation Times

The free induction decay (FID) of protons in API hydrates was obtained using a pulsed NMR spectrometer (25 MHz, JNM-MU25, JEOL, Tokyo, Japan). FID was obtained at 10, 20, 30, and 40°C. The 90° pulses were 2 μs in duration. The "solid echo," with an echo delay of 10 μs, was used in the detection stage of all measurements, in order to overcome the effects of the dead-time.[12] Measurement was repeated four times with a recycling time over five times of the T_1 value measured as described below.

The FID signals obtained between 2.6 and 100 μs that showed only Gaussian-type decay were fitted to Eq. (1) to calculate the T_2 of proton. FID signals obtained for quinidine sulfate and pipemidic acid hydrates showed a small diversion from Gaussian behavior (beat signal) in the final stage of relaxation, suggesting Abragam-type relaxation.[13] However, T_2 was calculated according to Eq. (1) for the purpose of comparison among API hydrates. The FID signals that show both Gaussian and Lorentzian decay patterns were fitted to Eq. (2) representing the summation of the Gaussian and Lorentzian equations.

$$I(t) = I_0 \exp\left[-\left(\frac{t}{T_2}\right)^2\right] \tag{1}$$

$$I(t) = I_0\left[P_G \exp\left(-\left(\frac{t}{T_{2(G)}}\right)^2\right) + P_L \exp\left(-\frac{t}{T_{2(L)}}\right)\right] \tag{2}$$

where $I(t)$ and I_0 are signal intensity at time t and time 0. $T_{2(G)}$ and $T_{2(L)}$ are T_2 for Gaussian decay and Lorentzian decay, respectively, and P_G and P_L are the proportion of protons that show Gaussian decay and Lorentzian decay, respectively.

The T_1 of proton in API hydrates was determined at 30°C by the inversion recovery method. T_1 was calculated according to Eq. (3).

$$I(t) = I_0\left(1 - 2\exp\left(-\frac{t}{T_1}\right)\right) \tag{3}$$

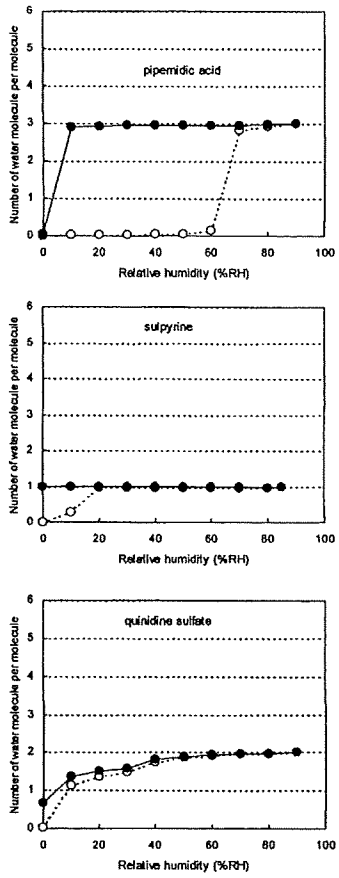

Figure 7. Water sorption isotherms for API hydrates showing a single endothermic peak in DSC thermogram.

Differential Scanning Calorimetry (DSC)

Modulated temperature DSC experiments were performed using a commercial system (2920; TA Instruments, New Castle, DE) attached to a refrigerated cooling accessory. The conditions were as follows: modulation period of 100 s, a modulation amplitude of ±0.5°C, and an underlying heating rate of 1°C/min. Temperature calibration was performed using indium. Samples (approximately 10 mg) were put in a pan without a lid. Nitrogen gas was flowed at 30 mL/min.

Water Sorption Isotherm

Water sorption isotherms were measured gravimetrically at 25°C using the automated sorption analyzer from VTI Corp. (Hialeah, FL). Prior to water sorption and desorption, samples were dried at 60°C and reduced pressure, until the partial vapor pressure became less than 0.0. Equilibrium water content was measured at ascending partial vapor pressures ranging from 0.10 to 0.95, then at descending partial vapor pressures ranging from 0.95 to 0.00 in steps of 0.10 or 0.05. Equilibrium was regarded to have been achieved once the change in sample weight was less than 0.001 mg over 10 min. The limit duration for measurement at a partial vapor pressure was 10 h for scopolamine hydrobromide and 5 h for the others.

RESULTS

NMR Relaxation Times

Figures 1 and 2 show representative examples of the time courses of spin–spin relaxation observed for the 11 API hydrates. Of the four antibiotic hydrates, all exhibited both Gaussian-type decay and Lorentzian decay, as exemplified by ceftazidime and cefazolin sodium hydrates (Fig. 1). The other seven API hydrates exhibited only Gaussian-type decay, as exemplified by quinidine sulfate and scopolamine hydrobromide hydrates (Fig. 2).

In order to calculate the proportion of water protons to API protons, which is required to obtain the T_2 of the water protons by curve-fitting of decay patterns, the number of water molecules per API hydrate molecule was measured by the Karl Fischer method. The results are shown in Table 1, in which the values specified in the JP are also noted for the purpose of comparison. The measured water contents were consistent with those specified in the JP for pipemidic acid, sulpyrine, and quinidine sulfate hydrates, as well as all antibiotic hydrates except for cefazolin sodium hydrate. In contrast, quinine hydrochloride, scopolamine hydrobromide, and saccharin sodium hydrates showed smaller water contents than those specified in the JP.

The time courses of spin–spin relaxation showing both Gaussian decay and Lorentzian decay observed for the four antibiotic hydrates were well fitted to Eq. (2) using the proportion of water protons calculated from the measured water

DOI 10.1002/jps

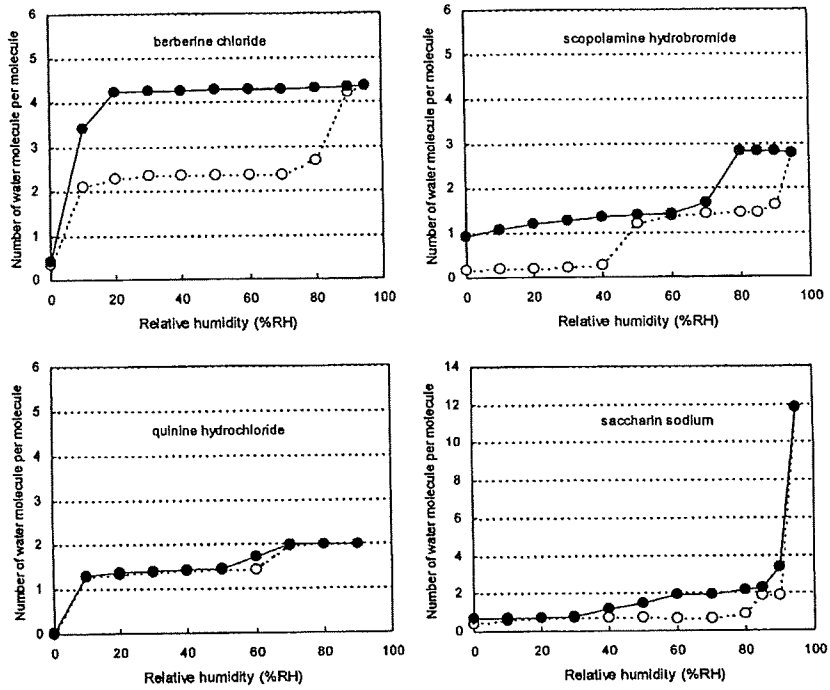

Figure 8. Water sorption isotherms for API hydrates showing two endothermic peaks in DSC thermogram.

content, as shown by the regression curve in Figure 1. Therefore, all of the water protons in the molecule are considered to show Lorentzian decay, and the Gaussian decay is attributed to the drug protons. The T_2 of the Lorentzian decay was calculated according to Eq. (2), and the results will be discussed below. For cefazolin sodium hydrate, better curve-fitting was obtained by regression analysis using a slightly larger value for the proportion of water protons than that calculated from the measured water content. This suggests that a small number of the drug protons exhibit Lorentzian decay; however, it is possible that the water content of the sample used for NMR measurement was different from that of the sample used for Karl Fischer measurements.

The seven API hydrates other than the antibiotic hydrates did not exhibit Lorentzian decay, indicating that all water protons and drug protons in the molecule showed Gaussian decay. The T_2 of the water protons was calculated according to Eq. (1), assuming that the T_2 of the drug protons is similar to that of the water protons. The results will be discussed below.

DSC Thermograms

Figures 3–5 show DSC thermograms measured for the 11 API hydrates. The four antibiotic hydrates, which exhibited Lorentzian decay upon spin–spin relaxation, showed a single endothermic peak due to water evaporation, as shown in Figure 3. In contrast, the API hydrates that did not exhibit Lorentzian decay showed two endothermic peaks (Fig. 4), or one peak (Fig. 5).

The temperature at which an endothermic peak due to water evaporation is observed may be considered to represent the ease of evaporation of hydration water under nonisothermal conditions. The onset temperature was determined as a parameter for approximate comparison of ease of evaporation among the API hydrates, along with ease of evaporation under isothermal conditions as

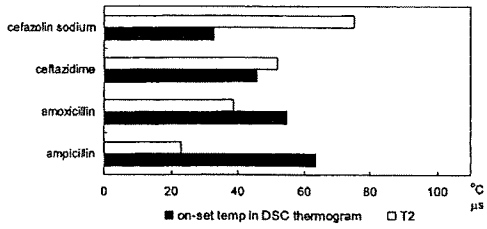

Figure 9. Correlation between onset temperature and T_2 for four antibiotic hydrates.

determined by water vapor sorption analysis. Onset temperature is known to depend on various factors, such as the heating rate, the shapes of the pan and lid, the surface area of the sample, and the flow rate of nitrogen gas. In this study, controllable factors such as the heating rate and the flow rate of nitrogen gas were kept constant, and a pan without a lid was used. The onset temperatures obtained will be discussed below.

Water Vapor Sorption Isotherm

Figures 6–8 show water sorption isotherms observed for the four antibiotic hydrates, the other three API hydrates that exhibited a single endothermic peak due to water evaporation, and the four API hydrates that exhibited two peaks due to water evaporation, respectively. The y-axis represents the number of water molecules per API hydrate molecule, calculated from the water content measured by the Karl Fischer method, assuming that all water molecules present in the sample were evaporated during the drying process (60°C, reduced pressure) prior to the sorption and desorption processes.

The water sorption isotherms (Fig. 6) observed for the four antibiotic hydrates, which exhibited Lorentzian decay upon spin–spin relaxation, indicate that during the desorption process, the water content decreased with decreasing humidity in the range 90–0% RH, with a significant slope in the water content versus humidity plot.

Among the three API hydrates that did not exhibit Lorentzian decay and showed a single endothermic peak due to water evaporation, pipemidic acid and sulpyrine hydrates gave water desorption isotherms in which the water content was constant over a wide humidity range, as shown in Figure 7. Quinidine sulfate also showed a flat line in the water content versus humidity plot, though it was observed only at high humidities.

The water desorption isotherms observed for the other four API hydrates (except berberine chloride), which did not exhibit Lorentzian decay and showed two endothermic peaks due to water evaporation, indicated that the water content remained approximately constant at two levels (Fig. 8).

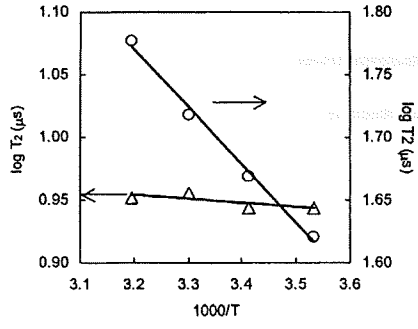

Figure 10. Temperature dependence of T_2 for ceftazidime (circle) and pipemidic acid (triangle) hydrates.

DISCUSSION

The molecular mobility of hydration water in API hydrates was found to vary over a wide range; some, such as ceftazidime hydrate, contain hydration water that shows Lorentzian decay upon spin–spin relaxation, while others contain hydration water that shows Gaussian decay.

Hydration Water Showing Lorentzian Decay

All of the water molecules present in the four antibiotic hydrates were found to exhibit Lorentzian decay, because the proportion of Lorentzian decay was consistent with the proportion of water protons calculated from the water content measured by the Karl Fischer method (Fig. 1). The finding that the water molecules in the antibiotic hydrates showed Lorentzian decay rather than Gaussian decay suggests that water molecules are held in voids in the crystal, rather than being firmly trapped in the crystal lattice. These water molecules may evaporate through channels formed in the interior of the crystal.[14] Hydration water that requires more energy to be released

DOI 10.1002/jps

may exhibit a higher onset temperature of the endothermic peak due to water evaporation in DSC.

The T_2 values determined based on Lorentzian decay is related with τ_c by Eq. (4), such that a smaller value of T_2 represents a larger τ_c (lower mobility).

$$\frac{1}{T_2} = \frac{\gamma^4 \hbar^2 I(I+1)}{5r^6}\left(3\tau_c + \frac{5\tau_c}{1+\omega_0^2\tau_c^2} + \frac{2\tau_c}{1+4\omega_0^2\tau_c^2}\right) \quad (4)$$

where γ, ω_0, I, r, and $\hbar$ are the gyromagnetic ratio, resonance frequency, spin quantum number, spin distance, and the Plank's constant divided by 2π.

As shown in Figure 9, T_2 increased as the onset temperature (Fig. 3) decreased, indicating that hydration water which evaporates at lower temperatures has greater molecular mobility as determined by T_2. This correlation between T_2 and the ease of evaporation under nonisothermal conditions may be explained by assuming that hydration water with a greater T_2 (higher mobility) can escape through channels at a lower temperature.

In order to gain further insight into the correlation between ease of evaporation and the molecular mobility of the hydration water, the ease of evaporation under isothermal conditions was evaluated by water sorption isotherm measurement. Each of the four antibiotic hydrates exhibited a desorption isotherm showing decreases in water content associated with decreases in humidity (Fig. 6). As discussed below, the crystal form of ampicillin hydrate appeared to be altered during the drying process prior to the measurement of water sorption isotherms. Therefore, the isotherm obtained for ampicillin could not be compared with the NMR and DSC data. However, such detrimental effect of predrying was not observed for the other three antibiotic hydrates. The negative water content observed after the desorption process for ceftazidime may be due to chemical degradation occurred under high-humidity conditions or incomplete evaporation of hydration water during predrying. Compared to amoxicillin hydrate, cefazolin sodium hydrate, which has a larger T_2 value, exhibited a greater slope in its water content versus humidity plot. Furthermore, cefazolin sodium exhibited rapid dehydration when humidity was decreased below 20% RH, whereas amoxicillin did not exhibit rapid dehydration until humidity was decreased below 10% RH. These findings suggest that the ease of evaporation of hydration water under isothermal conditions is correlated with molecular mobility as determined by T_2, which supports the conclusion obtained based on DSC measurement. For ampicillin, the slope of the water content versus humidity plot was greater than that of amoxicillin hydrate despite its lower molecular mobility as determined by T_2 and higher onset temperature. This suggests that the drying conditions prior to the sorption and desorption processes were inadequate, which may result in destruction of the crystalline structure. Thus, the isotherm obtained for ampicillin could not be compared with the NMR and DSC data.

As exemplified by ceftazidime hydrate (Fig. 10), T_2 increased significantly with increasing temperature, indicating that T_2 reflects the increases in molecular mobility associated with increases in temperature. Thus, molecular mobility can be considered to correlate with T_2. As shown in Figure 11, antibiotic hydrates with smaller T_2

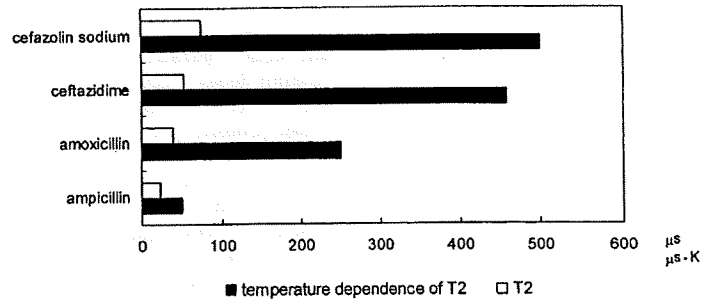

Figure 11. Correlation between T_2 and temperature dependence of T_2 for four antibiotic hydrates.

values showed a smaller change in T_2 with temperature change. This finding suggests that lower values of T_2 reflect a smaller scale of molecular motion, with lower activation energies.

Spin–lattice relaxation time (T_1) is known to reflect molecular mobility, similarly to T_2, but increases with decreasing T_2 (with decreasing molecular mobility) in the slow motional regime. The T_1 values of water protons in the presence of drug protons cannot be determined due to spin diffusion, but an approximate determination of T_1 for water protons is possible if the proportion of water protons is large. For example, in $Na_2HPO_4 \cdot 12H_2O$ and $Na_2HPO_4 \cdot 2H_2O$, water protons are predominant (24/25 and 4/5, respectively). $Na_2HPO_4 \cdot 12H_2O$ exhibits slower spin–spin relaxation (larger T_2) (Fig. 12), and faster spin–lattice relaxation (smaller T_1) (Fig. 13) compared to $Na_2HPO_4 \cdot 2H_2O$, which indicates that both T_1 and T_2 reflect the molecular mobility of hydration water. For the antibiotic hydrates examined, however, correlations between T_1 and T_2 were not observed, as shown in Figure 14. This finding indicates that for API hydrates containing a significant amount of drug protons, such as antibiotic hydrates, the molecular mobility of the hydration water is not reflected in T_1.

Hydration Water Showing Gaussian Decay

As mentioned previously, all of the API hydrates other than the four antibiotic hydrates exhibited only Gaussian decay (Fig. 2). The value of T_2 did not vary significantly among the API hydrates, as shown in Figure 15. Furthermore, the onset temperatures of the single endothermic peaks

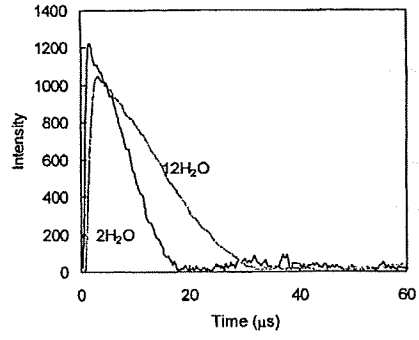

Figure 12. Free induction decay for Na_2HPO_4 $12H_2O$ and $2H_2O$.

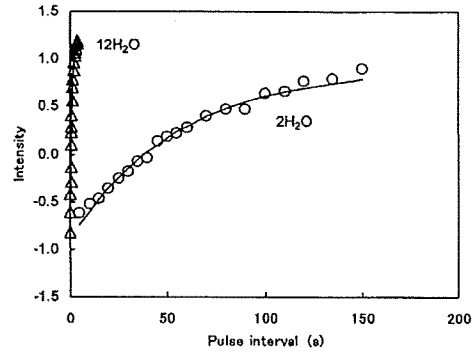

Figure 13. Spin–lattice relaxation for Na_2HPO_4 $12H_2O$ and $2H_2O$.

due to water evaporation for quinidine sulfate, pipemidic acid, and sulpyrine hydrates (Fig. 5), as well as each of the two peaks due to water evaporation observed for quinine hydrochloride, scopolamine hydrobromide, saccharin sodium, and berberine chloride hydrates (Fig. 4), were not correlated with T_2. These findings indicate that the molecular mobility of hydration water that shows Gaussian decay is too low to be reflected in T_2. No correlation between T_2 and molecular mobility is supported by the finding that changes in T_2 associated with changes in temperature were much smaller than those observed for the antibiotic hydrates that exhibited Lorentzian decay, as exemplified by pipemidic acid (Fig. 10). Such low molecular mobility may be attributed to water molecules firmly trapped in the crystal lattice, rather than water molecules trapped in voids in the crystal.

For quinidine sulfate, pipemidic acid, and sulpyrine hydrates, a single endothermic peak was observed in DSC (Fig. 5). The water content versus humidity plots showed a flat line at a certain number of water molecules. Pipemidic acid and sulpyrine showed a flat line at three and one water molecule(s) per hydrate, respectively, and evaporation of these water molecules was observed only under very low humidity (Fig. 7). These findings indicate that water molecules are firmly trapped in the crystal.

For quinine hydrochloride, scopolamine hydrobromide, saccharin sodium, and berberine chloride hydrates, two endothermic peaks were shown in DSC (Fig. 4). The water content versus humidity plots for these hydrates (except for berberine chloride) showed flat lines at two levels

DOI 10.1002/jps

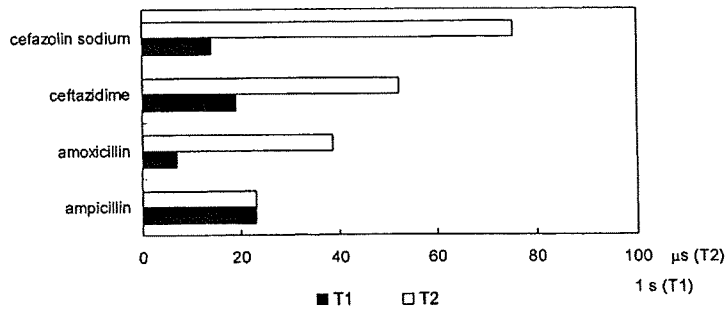

Figure 14. Correlation between T_1 and T_2 for four antibiotic hydrates.

of water content (Fig. 8), suggesting the presence of two water populations: molecules that evaporate at high humidity, and others that evaporate at lower humidity (below 10% RH). This seems to be consistent with the observation of two endothermic peaks in DSC. The endothermic peak observed at a high temperature and the flat line observed at a low humidity may be attributable to hydration water with strong hydrogen–bonding interactions, while the one observed at a lower temperature and higher humidity may be attributable to hydration water with week interactions. The presence of hydration water with week interactions is also supported by the finding that the water contents as measured by the Karl Fischer method were smaller than those specified in the JP (Tab. 1).

CONCLUSION

It was found that spin–spin relaxation time, T_2, is a useful parameter that can indicate the molecular mobility of water of hydration which has relatively high mobility and shows Lorentzian decay upon spin–spin relaxation. For these water molecules, molecular mobility as determined by T_2 is correlated with ease of evaporation both under nonisothermal and isothermal conditions,

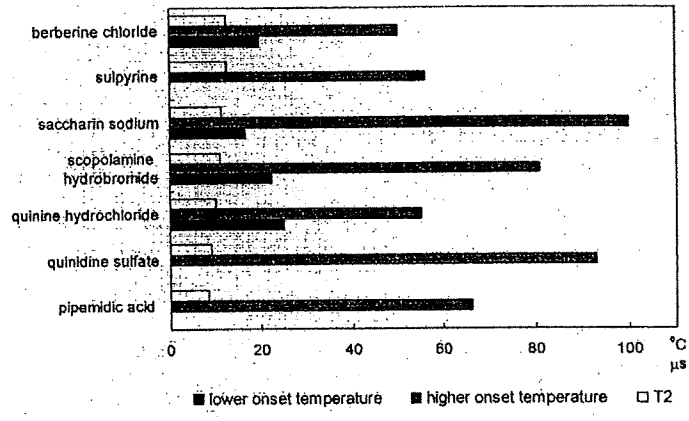

Figure 15. Correlation between onset temperature and T_2 for API hydrates that show Gaussian decay.

DOI 10.1002/jps

such that water molecules with greater ease of evaporation have higher T_2 values.

In contrast, for hydration water that has low mobility and shows Gaussian decay, T_2 was found not to correlate with ease of evaporation under nonisothermal conditions, suggesting that molecular motion that determines the ease of evaporation is not reflected in T_2; in this case, T_2 cannot be used as a parameter to indicate molecular mobility.

The water molecules in the API hydrates studied were found to have wide-ranging molecular mobilities, from low molecular mobility that could not be evaluated by NMR relaxation times, such as the water molecules in pipemidic acid hydrate, to high molecular mobility that could be evaluated by NMR relaxation times, such as the water molecules in ceftazidime hydrate.

REFERENCES

1. Yoshioka S, Aso Y. 2007. Correlations between molecular mobility and chemical stability during storage of amorphous pharmaceuticals. J Pharm Sci 96:960–981.
2. Ahlneck C, Zografi G. 1990. The molecular basis for moisture effects on the physical and chemical stabiity of drugs in the solid state. Int J Pharm 62:87–95.
3. Mimura H, Gato K, Kitamura S, Kitagawa T, Kohda S. 2002. Effect of water content on the solid-state stability in two isomorphic clathrates of cephalosporin: Cefazolin sodium pentahydrte (α form) and KF041 hydrate. Chem Pharm Bull 50: 766–770.
4. Zografi G. 1988. States of water associated with solids. Drug Dev Ind Pharm 14:1905–1926.
5. Newman AW, Reutzel-Edens SM, Zografi G. 2007. Characterization of the "hygroscopic" properties of active pharmaceutical ingredients. J Pharm Sci DOI: 10.1002/jps.21033.
6. Brittain HG, Grant DJW. 1999. Effect of polymorphism and solid state solvation on solubility and dissolution rate. In: Brittain HG, editor. Polymorphism in pharmaceutical solids. New York: Marcel Dekker. pp 279–330.
7. Shinyashiki N, Asaka N, Mashimo S. 1990. Dielectric study on dynamics of water in polymer matrix using a frequency range 10^6–10^{10} Hz. J Chem Phys 93:760–764.
8. Ahlqvist MU, Taylor LS. 2002. Water dynamics in channel hydrates investigated using H/D exchange. Int J Pharm 241:253–261.
9. Ruan R, Chen PL. 1998. Mobility of water in food and biological systems. In: Water in foods and biological materials, a nuclear magnetic resonance approach. Lancaster, PA: Technomic Publishing Company, Inc. pp 149–228.
10. Oksanen CA, Zografi G. 1993. Molecular mobility in mixtures of absorbed water and solid poly(vinylpyrrolidone). Pharm Res 10:791–799.
11. Otsuka T, Yoshioka S, Aso Y, Kojima S. 1995. Water mobility in aqueous solutions of macromolecular pharmaceutical excipients measured by oxygen-17 nuclear magnetic resonance. Chem Pharm Bull 43:1221–1223.
12. Mansfield P. 1965. Multiple-pulse nuclear magnetic resonance transients in solids. Phys Rev 137:A961–A974.
13. Parizel N, Meyer G, Weill G. 1993. Nuclear magnetic resonance linesahape studies of interpenetrating polymer networks. Polymer 12:2495–2502.
14. Morris KR. 1999. Structural aspects of hydrates and solvates. In: Brittain HG, editor. Polymorphism in pharmaceutical solids. New York: Marcel Dekker. pp 125–181.

Available online at www.sciencedirect.com
ScienceDirect
International Journal of Pharmaceutics 354 (2008) 196–203
INTERNATIONAL JOURNAL OF PHARMACEUTICS
www.elsevier.com/locate/ijpharm

Pharmaceutical Nanotechnology

Hydroxyethylated cationic cholesterol derivatives in liposome vectors promote gene expression in the lung

Wuxiao Ding[a], Yoshiyuki Hattori[a], Kimio Higashiyama[b], Yoshie Maitani[a,*]

[a] *Fine Drug Targeting Research Laboratory, Institute of Medicinal Chemistry, Hoshi University, Ebara 2-4-41, Shinagawa-ku, Tokyo 142-8501, Japan*
[b] *Synthetic Organic Chemistry Research Laboratory, Institute of Medicinal Chemistry, Hoshi University, Ebara 2-4-41, Shinagawa-ku, Tokyo 142-8501, Japan*

Received 25 July 2007; received in revised form 27 September 2007; accepted 21 October 2007
Available online 21 December 2007

Abstract

Three cationic cholesterol derivatives (CCDs), which differ in their types of amine and bear a hydroxyethyl group at the amine group, were synthesized and formulated into liposomes and nanoparticles as gene delivery vectors. *In vitro* transfection into A549 cells proved that liposomes formulated with CCDs and dioleoylphosphatidylethanolamine (DOPE) of 1/2 molar ratio were more effective than the corresponding nanoparticles with CCDs and Tween 80 at charge ratios (+/−) of 1/2, 3/1 and 5/1. Among the liposomal formulations, non-hydroxyethylated CCDs were more effective than hydroxyethylated ones *in vitro*. However, gene transfection in the lung through intratracheal injection showed opposite results to those *in vitro*, with liposomes containing hydroxyethylated CCDs being more potent than those containing non-hydroxyethylated CCDs. Transfection by liposomes with *N,N*-methyl hydroxyethyl aminopropane carbamoyl cholesterol iodide (MHAPC) showed the highest luciferase activity, resulting in 2- and 60-fold higher gene expression than jet-PEI and naked DNA, respectively. The distribution of MHAPC lipoplex after intratracheal injection was heterogeneous, and luciferase was expressed in epithelial cells lining the bronchi and bronchioles. All the lipoplexes led to higher TNF-α levels in the lung compared to the nanoplex and jet-PEI, but our findings suggested that modification of the cationic cholesterol with a hydroxyethyl group at the tertiary amine terminal, MHAPC, promoted gene expression in the lung without increasing the toxicity compared with other CCDs. This work firstly proved that liposomes containing hydroxyethylated CCDs could promote gene expression in the lung through intratracheal injection.

Keywords: Cationic liposomes; Nanoparticles; Intratracheal injection; Cationic cholesterol derivatives; Hydroxyethyl group

1. Introduction

Gene therapy in the lung still holds promise as an effective method for treating cystic fibrosis and lung neoplastic disease (Hoag, 2005). Gene delivery vectors are classified into viral and non-viral ones, and both of them have been well studied. Cationic lipids (Miller, 2003) and polymers (Pietersz et al., 2006), which can compact negatively charged genetic materials through electrostatic interaction and transport them into the cells, constitute a large fraction of non-viral vectors. Many cationic lipids have been reported to mediate gene delivery *in vitro* and *in vivo* (Miller, 2003), and more are being reported all the time.

After the discovery of 3β-[*N*-(*N'*,*N'*-dimethylaminoethane) carbamoyl] cholesterol (DC-Chol) (Gao and Huang, 1991), many effective cationic cholesterol derivatives (CCDs) were soon developed (Ghosh et al., 2002; Hasegawa et al., 2002; Miller, 2003; Nakanishi, 2003; Percot et al., 2004; Bajaj et al., 2007). CCDs are amphiphilic molecules that consist of a cationic headgroup attached via a linker to the cholesteryl skeleton. Clearly, the linker and the cationic headgroup are crucial for the gene transfection ability and toxicity. The inability of CCD-containing cationic liposomes to produce persistent gene expression (Scheule et al., 1997) results in a need for repeated dosing of the liposomes. Therefore, biodegradable CCDs with a linker such as carbamate ester, which can facilitate degradation *in vivo*, are strongly recommended for the design and synthesis of CCDs (Choi et al., 2001). In fact, this strategy has already been verified to be effective by the low toxicity of DC-Chol (Gao and Huang,

* Corresponding author. Tel.: +81 3 5498 5048; fax: +81 3 5498 5048.
E-mail address: yoshie@hoshi.ac.jp (Y. Maitani).

0378-5173/$ – see front matter © 2007 Elsevier B.V. All rights reserved.
doi:10.1016/j.ijpharm.2007.10.051

1991) and cationic 3β-[L-lysinamide-carbamoyl]cholesterol derivatives (K-Chol) (Choi et al., 2001; Lee et al., 2006).

Moreover, the amine headgroups of cationic lipids definitely determine their transfection ability (Reynier et al., 2004). Among various amine headgroups, hydroxyethyl group-containing ones have exhibited higher gene transfection than the corresponding hydroxyethyl-lacking ones (Okayama et al., 1997; Venkata Srilakshmi et al., 2002; Arpicco et al., 2004). Cholesteryl-3β-carboxyaminoethylene-*N*-hydroxyethylamine (OH-Chol) is a cationic cholesterol with a hydroxyethyl group at the amine headgroup, linked to the cholesteryl skeleton by an amido bond. Liposomes containing OH-Chol and phosphatidylethanolamine (DOPE) showed high gene transfection ability (Okayama et al., 1997). Furthermore, a nanoparticle formulation with OH-Chol exhibited excellent gene transfection. Their high gene transfection activity was ascribed to the hydroxyethyl group at the cationic headgroup of OH-Chol (Hattori et al., 2007). The combination of a hydroxyethyl group at the headgroup and amine lipids, therefore, will produce effective cationic carbamate-linked lipids for gene delivery vectors.

To develop highly potent and biodegradable CCDs, in this study, we synthesized three types of CCDs bearing secondary, tertiary and quaternary amines, with a carbamate ester linker and a hydroxyethyl group at the amine headgroup. The synthesized CCDs were formulated into nanoparticles and liposomes, and their formulations were optimized for gene transfection of the human lung adenocarcinoma A549 cell line and into the mouse lung through intratracheal injection. The location of luciferase expression was studied by immunohistochemistry. Furthermore, the inflammatory response of the nanoplexes and lipoplexes was evaluated.

2. Materials and methods

2.1. Materials and instrumentation

DC-Chol and cholesterol chloroformate were purchased from Sigma–Aldrich (St. Louis, USA). *N,N*-Dimethyl-1,3-propanediamine; *N*-methyl-1,3-propanediamine; 1,3-propanediamine; 2-iodoethanol were purchased from Wako Pure Chemistry (Osaka, Japan). Tween 80 was obtained from NOF Co. Ltd. (Tokyo, Japan) and DOPE was from Avanti Polar Lipids Inc., (Alabaster, AL, USA). The synthesis of OH-Chol was done as previously reported (Hattori et al., 2005). RPMI-1640 culture medium was purchased from Invitrogen Corp. (Carlsbad, CA, USA). ^{1}H NMR (270 MHz) and ^{13}C NMR (67.8 MHz) spectra were recorded using tetramethylsilane as an internal standard with a JEOL JNM-LA270 spectrometer. Chemical ionization (CI) was carried out on JEOL JMS 600 (JEOL, Tokyo, Japan). The plasmid pCMV-luc encoding the luciferase gene under the control of the CMV promoter was constructed as previously described (Igarashi et al., 2006). A protein-free preparation of the plasmid was purified following alkaline lysis using Maxiprep columns (Qiagen, Hilden, Germany).

2.2. Synthesis of cationic cholesterol derivatives (Fig. 1)

2.2.1. N,N,N-Dimethyl aminopropane carbamoyl cholesterol iodide (DMAPC, 1) and N,N,N-dimethyl hydroxyethyl aminopropane carbamoyl cholesterol iodide (DMHAPC, 2)

1 was synthesized as described by Percot et al. (2004) and hydroxyethylated to **2** with some modifications. **1** and iodoethanol were refluxed in toluene (with a catalytic amount of DMF) at 105 °C for 24 h. Silica-gel chromatography with $CHCl_3$/methanol for elution gave **2** (yield 70%), a pale yellow powder.

2.2.2. N-Hydroxyethyl aminopropane carbamoyl cholesterol iodide (HAPC, 3)

A solution of cholesterol chloroformate (2.7 g, 6 mmol) in 10 ml of dry dichloride methylene (DCM) was slowly added to a pre-cooled solution of 1,3-propanediamine (5 ml, 60 mmol) in 100 ml of DCM. The mixture was further stirred at RT for 1 h. After the reaction, the solvent was removed by vacuum evaporator and the residue was purified on silica gel to give aminopropane carbamoyl cholesterol (2.8 g, 95%). 2.8 g (5.75 mmol) of aminopropane carbamoyl cholesterol was dissolved in a mixture of DCM/methanol with 1 equiv. of triethylamine, and iodoethanol (1.9 mmol, 150 μl) was added and

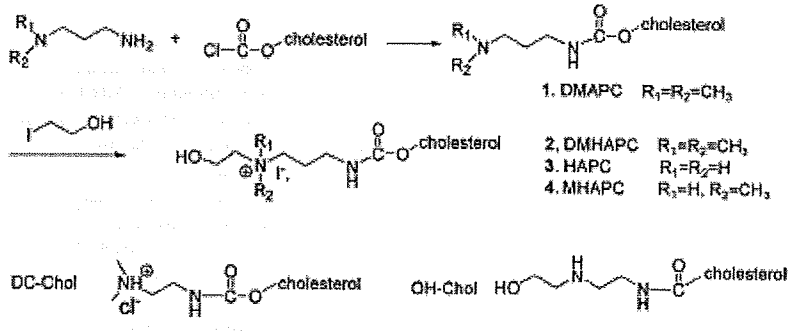

Fig. 1. Chemical structures and synthesis of cationic cholesterol derivatives.

stirred at RT for 24 h. Careful purification on silica-gel chromatography with $CHCl_3$/methanol for elution gave **3** (1.2 g, 31%). ^1H NMR ($CDCl_3$) δ: 7.62 (s, 1H, –CO–NH–C), 5.36 (t, 3H, C=CH–C), 4.41 (m, 1H, CH–O–CO–), 4.1 (m, 2H, –C–CH_2–O). ^{13}C NMR ($CDCl_3$) δ: 157.2 (NH–CO–O), 139.5, 122.5 (C=CH), 74.9 (=CH–O), 64.9 (–CH_2–OH). CI-MS *m/z*: found 658 (Calcd for $C_{33}H_{59}IN_2O_3$, 658.36).

2.2.3. *N,N-Methyl hydroxyethyl aminopropane carbamoyl cholesterol iodide (MHAPC, 4)*

Similarly to **3**, **4** (3.6 g, 94%) was synthesized from *N*-methyl-propanediamine (3.7 ml, 30 mmol) and cholesterol chloroformate (2.7 g, 6 mmol) and subsequently hydroxyethylated with iodoethanol (6.84 mmol, 540 μl). ^1H NMR ($CDCl_3$) δ: 7.91 (s, 1H, –CO–NH–C), 5.36 (t, 3H, C=CH–C), 4.41 (m, 1H, CH–O–CO–), 4.1 (m, 2H, –C–CH_2–O), 2.92 (s, 3H, CH_3–N^+). ^{13}C NMR ($CDCl_3$) δ: 158.1 (NH–CO–O), 139.2, 122.8 (C=CH), 74.8 (=CH–O), 63.2 (–CH_2–OH). CI-MS *m/z*: found 673 (Calcd for $C_{34}H_{61}IN_2O_3$, 672.37).

2.3. *Preparation of liposomes/lipoplexes and nanoparticles/nanoplexes*

The synthesized CCDs, namely DMAPC, DMHAPC, HAPC and MHAPC, together with DC-Chol and OH-Chol (Fig. 1), were formulated into liposomes with DOPE and into nanoparticles with 5% Tween 80 by a modified ethanol injection method (Hattori et al., 2005). The molar ratio of CCDs to DOPE in the liposomes was varied from 2/1 to 1/1 to 1/2. Each type of liposomes and nanoparticles contained 0.9 mM CCD lipid concentration for *in vitro* transfection and 4.5 mM for *in vivo* experiments.

The CCD liposome/DNA complex (CCD lipoplex) and CCD nanoparticle/DNA complex (CCD nanoplex) for *in vitro* transfection at various charge ratios (+/−) of CCD to DNA were prepared by addition of each liposome or nanoparticle preparations (1.67, 10, 16.7 μl for the charge ratio (+/−) of 1/2, 3/1 and 5/1) to 1 μg of DNA in 5 μl of MilliQ water with 10 rounds of pipetting. After the preparations were left at room temperature for 15 min, the size of each lipoplex/nanoplex in water was measured after incubation with RPMI-1640 medium for a further 15 min. The mean particle size was measured by the dynamic light scanning method (ELS-Z2, Otsuka Electronics Co. Ltd., Osaka, Japan). For the *in vivo* study, the lipoplexes and nanoplexes at charge ratio (+/−) of 3/1 were prepared by the addition of 40 μl of liposomes or nanoparticles, respectively to 20 μg of DNA in 25 μl of MilliQ water. The total injection volume was fixed at 65 μl per mouse.

2.4. *Cell culture*

The human lung adenocarcinoma A549 cell line was kindly provided by OncoTherapy Science, Inc. (Kanagawa, Japan). The cells were maintained in RPMI-1640 medium supplemented with 10% FBS and kanamycin (100 μg/ml) at 37 °C in a 5% CO_2 humidified incubator.

2.5. *Gene transfection in A549 cell line and in the lung*

For transfection into A549 cells, the lipoplexes or nanoplexes were diluted in 500 μl of 10% FBS supplemented RPMI-1640 and then incubated with the cells in 12-well plates for 24 h. As a positive control, the Lipofectamine 2000 (LA2000, Invitrogen Corp.)/DNA complex was prepared according to the manufacturer's protocol.

To study the gene expression in the mouse lung, intratracheal injection through the exposed trachea was used as an injection method. Briefly, a ddY mouse (male, 5 weeks of age, Sankyo Lab., Shizuoka, Japan) was anesthetized with phenobarbital sodium (50 μg/g body weight) by intraperitoneal injection (i.p.). Then the mouse was positioned in a vertical position and the trachea was exposed by blunt dissection of the neck. Sixty-five microliters of complex suspension per mouse was bolus injected into the trachea using a 29G injection syringe. The jet-PEI (polyplus-transfection, NY, USA)/DNA complex was prepared at a (+/−) ratio of 5/1 according to the manufacturer's instructions.

2.6. *Luciferase assay and TNF-α in the lung tissue*

Luciferase expression in A549 cells was measured as counts per second (cps)/μg total protein using the luciferase assay system (Picagene, Tokyo Ink Mfg. Co. Ltd., Tokyo, Japan) and BCA reagent (Pierce, IL, USA) as previously described (Maitani et al., 2007).

The luciferase in the lung was measured 24 h after intratracheal injection. Mice were anesthetized with ethyl ether and the lung was perfused with 10 ml of PBS through the left ventricle to remove the blood. The lung was collected with minimal main bronchi and immediately homogenized in 500 μl of cold lysis buffer (Promega Co., Madison, WI, USA). The homogenate samples were centrifugated at 15,000 rpm for 5 min at 4 °C and the luciferase assay was done as described above.

For TNF-α measurement, lysates were prepared exactly as described for the luciferase assay in the lung. TNF-α levels were determined using a mouse TNF-α ELISA kit (R&D, Minneapolis, MN, USA).

2.7. *Immunohistochemistry of luciferase in the lung*

0.01% (molar percentage of lipids) rhodamine-DHPE (*N*-(lissamine rhodamine B sulfonyl)-1,2-dihexadecanoyl-*sn*-glycero-3-phosphoethanolamine, triethylammonium salt) labeled MHAPC liposomes (MHAPC/DOPE=1/2, molar ratio) were prepared with MHAPC concentration of 4.5 mM as described in Section 2.3. The lipoplex was prepared with 20 μg of DNA at a charge ratio (+/−) of 3/1. The lipoplexes were intratracheally injected into mouse lung, and the lung was collected at 24 h. The frozen lungs were cryosectioned into 12 μm slices. The sections were fixed with 70% ethanol and washed in PBS before incubation with primary goat anti-luciferase pAb (1:100) (Promega Co.). The sections were then incubated in bovine serum albumin (BSA) to reduce non-specific binding of a secondary antibody. Finally, they were incubated with rabbit

anti-goat IgG–HRP (Santa Cruz Biotech, Santa Cruz, CA, USA) for 2 h. The color was developed using a peroxidase substrate kit DAB SK-400 (Vector Lab, Inc. Burlingame, CA, USA).

3. Results and discussion

3.1. DOPE content in liposomes affected gene transfection

DOPE played a very important role in the destabilization of liposomes upon contact with cellular membranes and/or endosomes. In the formulations of cationic liposomes containing DOPE as a helper lipid, most studies used cationic lipids/DOPE at a molar ratio of 2/1, 3/2 or 1/1 as the optimum formulation (Miller, 2003). Recently we reported that DC-Chol/DOPE (1/2, molar ratio) liposomes, which were prepared by a modified ethanol injection method, were more effective for gene transfection than DC-Chol/DOPE = 1/1 and 3/2 liposomes (Maitani et al., 2007). To optimize the CCD liposomes, therefore, at first the DOPE content in liposomes was investigated in an attempt to determine the most effective formulations. As shown in Fig. 2, all the lipoplexes showed higher gene transfection in A549 cells with increasing molar ratio of DOPE (CCD/DOPE = 1/2, molar ratio) at a charge ratio (+/−) of 3/1, lipoplexes with less DOPE content (CCD/DOPE = 1/1 and CCD/DOPE = 2/1) were not effective enough to transfect A549 cells. Therefore, a liposome formulation rich in DOPE content, CCD/DOPE = 1/2-liposomes, was used for further studies. The lipoplexes were named DC-Chol, DMAPC, DMHAPC, HAPC and MHAPC lipoplexes.

3.2. Characterization of lipoplexes and nanoplexes

Although liposomes rich in DOPE had higher gene transfection ability than those poor in DOPE, they were only 1/10 to 1/50 as effective as LA-2000 (Fig. 2). Since a nanoparticle formulation with OH-Chol and Tween 80 has shown excellent gene transfection (Hattori et al., 2007), we prepared CCD nanoparticles using Tween 80 as well as CCD liposomes and investigated their use for gene transfection in A549 cells at three charge ratios (+/−) of 1/1, 3/1 and 5/1.

The liposomes and nanoparticles prepared by modified ethanol injection had a mean particle size of about 200 nm, with zeta-potential from +40 to +60 mV, except for OH-Chol/DOPE (1/2, molar ratio) liposomes, which were about 400 nm in size.

To establish the relationship between gene transfection and particle size, the size of lipoplexes (Fig. 3A) and nanoplexes (Fig. 3B) was measured after incubation with RPMI-1640 culture medium. CCD lipoplexes or nanoplexes showed a mean

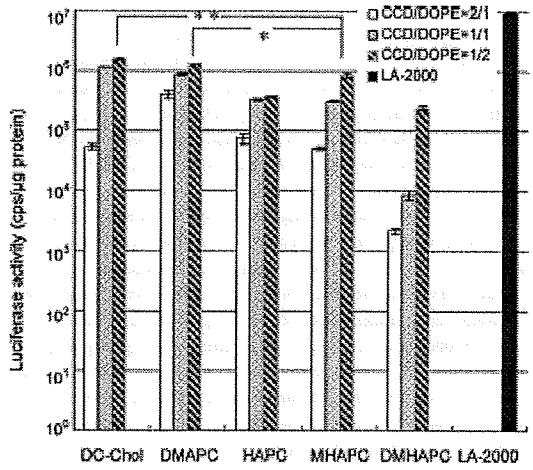

Fig. 2. Effect of DOPE composition in CCD lipoplexes on transfection efficiencies. LA-2000 is lipofectamine-2000. Charge ratio (+/−) was 3/1 and the amount of DNA was 1 μg/well. The values are expressed as mean ± S.D. ($n = 3$). *$P < 0.05$, **$P < 0.01$, Student's t test.

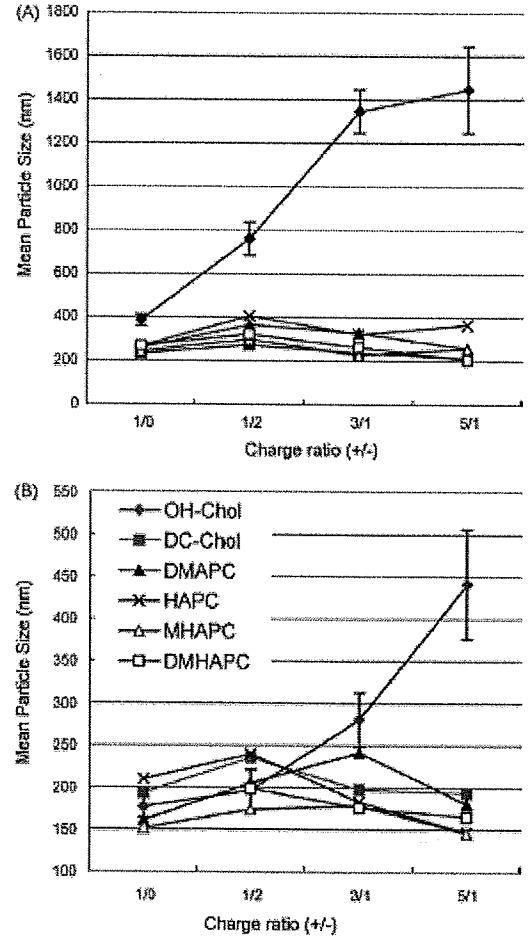

Fig. 3. Particle size of lipoplexes (A) and nanoplexes (B) after incubation with RPMI-1640 medium. The size of each lipoplex and nanoplex in water was measured after incubation with RPMI-1640 medium for 15 min. The values for OH-Chol were expressed as mean ± S.D., other values are expressed as mean values ($n = 3$).

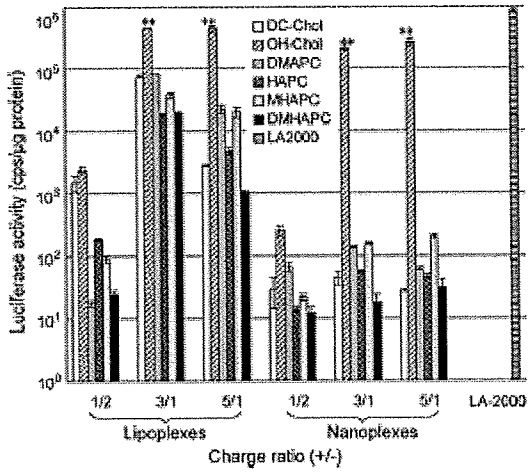

Fig. 4. Transfection efficiencies of lipoplexes and nanoplexes in A549 cells. The values were expressed as mean ± S.D. ($n=3$). **Significant difference between OH-Chol and other CCDs in the same charge ratio group ($P<0.01$, Student's t test). The values are expressed as mean ± S.D. ($n=3$).

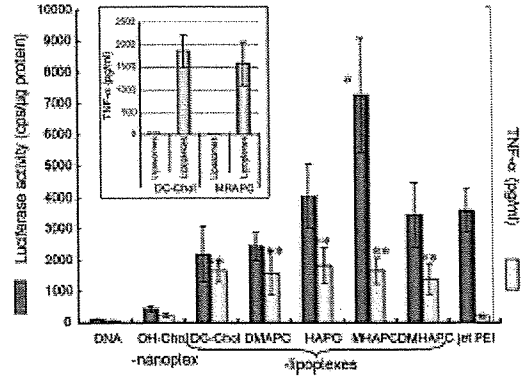

Fig. 5. Luciferase activity (closed columns) and TNF-α (open columns) in the lung at 24 h after intratracheal injection of lipoplexes and nanoplexes (+/− = 3/1). *Significant difference from OH-Chol nanoplex, jet-PEI, DC-Chol and DMHAPC lipoplexes ($P<0.05$, Student's t test). **Significant difference from OH-Chol nanoplex and jet-PEI ($P<0.01$, Student's t test). The values are expressed as mean ± S.D. ($n=3$). The inset showed the TNF-α values of DC-Chol and MHAPC liposomes or lipoplexes in the lung at 24 h after intratracheal injection.

particle size from 150 to 300 nm at a charge ratio (+/−) of 3/1. The OH-Chol liposomes and nanoparticles formed large particles with DNA at charge ratios (+/−) of 3/1 and 5/1, and, therefore, for the *in vivo* study, we selected OH-Chol nanoplexes only at a charge ratio (+/−) of 3/1 as the optimum formulation.

3.3. Comparison between lipoplexes and nanoplexes for gene transfection in A549 cells

As shown in Fig. 4, the lipoplexes were far more effective than nanoplexes at the same charge ratio, especially at charge ratios (+/−) of 3/1 and 5/1. This may be explained by the contribution of the membrane destabilization role of DOPE in the liposomes. Among the six kinds of cationic cholesterol derivatives, OH-Chol lipoplexes and nanoplexes exhibited significantly elevated gene transfection, which may have been due to many factors, such as the amido linker and hydroxyethyl group in the structure of OH-Chol (Okayama et al., 1997), and some physical characteristics of the OH-Chol lipoplex and nanoplex, such as large particle size as shown in Fig. 3. The large particle size of OH-Chol lipoplex and nanoplex contributed partly to the high gene transfection in A549 cells, since large particles were more readily endocytosized into cells.

Furthermore, by comparing various lipoplexes at a charge ratio (+/−) of 3/1, we can see that the non-hydroxyethylated cationic cholesterol derivatives, DC-Chol and DMAPC, were more effective than hydroxyethylated ones (except for OH-Chol), namely DMHAPC, HAPC and MHAPC. Moreover, MHAPC, which bears a tertiary amine in the headgroup, exhibited a little higher transfection ability than HAPC and DMHAPC at the optimized formulation (CCD/DOPE = 1/2, molar ratio). Based on the higher gene transfection of lipoplexes than nanoplexes in A549 cells, we selected lipoplexes at a charge ratio (+/−) of 3/1 for further *in vivo* research.

3.4. Luciferase expression and TNF-α levels in the lung

Bolus intratracheal injection through the exposed bronchui of mouse was employed for all the *in vivo* studies. This administration method guarantees that 100% of the injected solution reaches the lung instantly (Driscoll et al., 2000). As long as the lipoplexes and nanoplexes can be stabilized under the mucus during distribution of the suspension in the lung, they have a chance to transfect the epithelial cells and even the alveolar cells in the lung.

As shown in Fig. 5, use of the lipoplexes resulted in much higher gene expression in the lung than use of OH-Chol nanoplexes, which were the most effective in A549 cells. One possible reason for this may be the insufficient DNA-protecting ability of OH-Chol nanoplexes in the presence of mucus and surfactants in the lung, while the lipoplexes might be able to encapsulate DNA in highly ordered multilammellar structures. Among these lipoplexes, DMHAPC, HAPC, and MHAPC lipoplexes, which were all hydroxyethylated in the cationic terminal, showed higher luciferase level than DC-Chol and DMAPC lipoplexes, which were not hydroxyethylated. In contrast to the *in vitro* data, the lipoplexes containing hydroxyethylated cationic cholesterol derivatives most strongly promoted gene expression in the lung. Although it is unclear how a hydroxyethyl group at the amine headgroup improves transfection, the hydroxyethyl moiety may affect the interaction between DNA and the cationic lipid membrane, and assist cellular association or some steps after internalization into the cells (Nakanishi and Noguchi, 2001).

Interestingly, the use of MHAPC lipoplexes, which contained a hydroxyethylated tertiary amine as the cationic part, resulted in 2- and 60-fold higher gene expression than the use of jet-PEI and naked DNA, respectively. The exact mechanism by which

the hydroxyethyl group in the cationic part and the tertiary amine in MHAPC increased gene expression is not known, but might be related to the stability of MHAPC lipoplexes in the presence of mucus and/or increased release of DNA from the lipoplexes in the acidic endosomal compartment.

Although the use of lipoplexes resulted in much higher gene expression in the lung, the lung seemed to have some inflammatory response to the lipoplex suspensions. The lipoplexes induced higher TNF-α secretion than OH-Chol nanoplexes and jet-PEI. The strong inflammatory response to lipoplexes was thought to be related to the lipoplexes themselves, since only low levels of TNF-α were detected with the DNA alone and DC-Chol and MHAPC liposomes alone (Fig. 5, inset). Furthermore, the high DOPE content in the lipoplexes might also have been responsible for the inflammatory response, since both OH-Chol nanoplexes and MHAPC nanoplexes induced low levels of TNF-α (data not shown). The present data were in accord with a report showing that lung toxicity observed with lipoplexes could be increased by the addition of DOPE, although DOPE suspension alone caused a negligible inflammatory response (Scheule et al., 1997).

3.5. Charge ratio of MHAPC lipoplex affected gene transfection

As shown in Fig. 3, the positively charged (+/− = 3/1) MHAPC lipoplexes were far more effective than negatively charged ones (+/− = 1/2) in A549 cells. Since most reports showed that nearly neutral or negatively charged lipoplexes/nanoplexes can produce higher gene expression in tumor tissues than positively charged ones (Miller, 2003; Hattori et al., 2007), we investigated the effect of the charge ratio (+/−) of MHAPC lipoplexes on gene transfection in the lung. In Fig. 6, it can be seen very clearly that the *in vivo* result corresponded to the *in vitro* one, with positively charged (+/− = 3/1) lipoplexes being significantly more effective than negatively charged ones. Since there are large amounts of surfactants and proteins in the lung lavage fluids and much mucin covers the epithelial cells in the lung, negatively charged lipoplexes might have a small chance of being retained as intact particles to transfect epithelial cells, whereas positively charged lipoplexes might be stable enough to exhibit gene expression ability (Rosenecker et al., 2003).

3.6. Distribution of MHAPC lipoplexes in the lung and localization of luciferase by immunostaining

Since MHAPC lipoplexes at a charge ratio (+/−) of 3/1 produced the highest gene expression in the lung, we investigated the distribution of rhodamine-labeled MHAPC lipoplexes and the location of the luciferase expression they produced after intratracheal injection. By observing the fluorescence of rhodamine in the cryosections, it was clear that rhodamine was mainly distributed throughout the bronchi and bronchioles, and some had even diffused to the alveolar cells (Fig. 7a and b). However, the distribution of lipoplexes was not homogeneous throughout the lungs: no fluorescence of rhodamine was

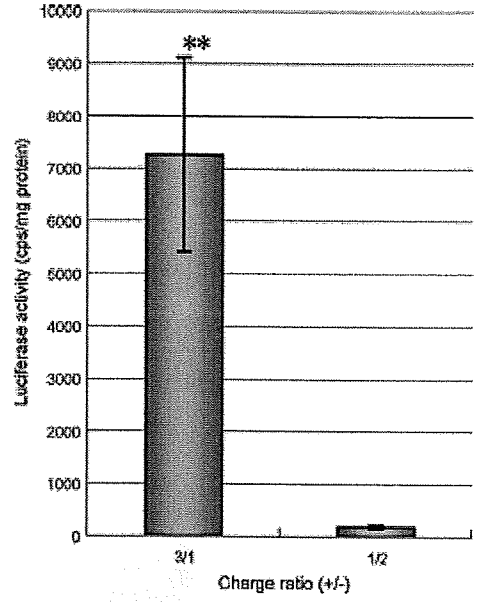

Fig. 6. Effect of charge ratio (+/−) of MHAPC lipoplexes on gene expression in the lung. **, Significant difference ($P<0.01$, Student's t test). The values are expressed as mean ± S.D. ($n=3$).

observed in some other regions in the same slice (Fig. 7c and d). From the morphological observation of the lungs which received the MHAPC lipoplex suspension, only the upper and middle lobes exhibited an increased inflammatory response compared to normal lung tissue, indicating that the intratracheally injected lipoplex was mainly located in the upper and middle lobes (photos not shown).

After luciferase immunostaining (Fig. 7e–h), the fluorescence of rhodamine was markedly decreased after many rounds of washing. The fluorescence was only located in the epithelial cells of the bronchi and bronchioles (Fig. 7f and h), and luciferase was also only expressed in the epithelial cells (Fig. 7e, arrows). Although some fluorescence of rhodamine was seen in the alveolar cells (Fig. 7b), there was no luciferase expression in the alveolar cells (Fig. 7e). We suppose that the fluorescence in the alveolar cells was mainly caused by free rhodamine-DHPE that became separated from the lipoplexes in the lung.

Lipoplexes administered by intravenous injection can be captured by the vascular system in the lung and induce gene expression in the lung alveolar region (Scheule et al., 1997). Since intratracheal injection has limited injection volume (1–2 ml/kg weight), the injected lipoplexes are directly exposed to the mucus around the bronchi and bronchioles, resulting in gene expression only in the epithelial cells lining the bronchi and bronchioles. This mode of injection, however, avoids gene expression in other organs, making it possible to decrease the dose of lipoplexes and possibly to decrease toxic side effects, and provides a potentially effective way for gene therapy of cystic fibrosis and other lung diseases.